ADVANCES IN ATMOSPHERIC SCIENCES, VOL. 33, DECEMBER 2016, 1329–1342

Simulation by CMIP5 Models of the Atlantic Multidecadal Oscillation and Its Climate Impacts

Zhe HAN[1], Feifei LUO*[2], Shuanglin LI[2], Yongqi GAO[2,3], Tore FUREVIK[4], and Lea SVENDSEN[3]

[1]*Key Laboratory of Regional Climate–Environment for Temperate East Asia, Chinese Academy of Sciences, Beijing* 100029, *China*

[2]*Nansen-Zhu International Research Centre and Climate Change Research Center, Institute of Atmospheric Physics, Chinese Academy of Sciences, Beijing* 100029, *China*

[3]*Nansen Environmental and Remote Sensing Center and Bjerknes Centre for Climate Research, Bergen* 5006, *Norway*

[4]*Geophysical Institute, University of Bergen and BjerknesCentre for Climate Research, Bergen* 5007, *Norway*

(Received 15 December 2015; revised 18 June 2016; accepted 8 July 2016)

ABSTRACT

This study focuses on the climatic impacts of the Atlantic Multidecadal Oscillation (AMO) as a mode of internal variability. Given the difficulties involved in excluding the effects of external forcing from internal variation, i.e., owing to the short record length of instrumental observations and historical simulations, we assess and compare the AMO and its related climatic impacts both in observations and in the "Pre-industrial" experiments of models participating in CMIP5. First, we evaluate the skill of the 25 CMIP5 models' "Historical" simulations in simulating the observational AMO, and find there is generally a considerable range of skill among them in this regard. Six of the models with higher skill relative to the other models are selected to investigate the AMO-related climate impacts, and it is found that their "Pre-industrial" simulations capture the essential features of the AMO. A positive AMO favors warmer surface temperature around the North Atlantic, and the Atlantic ITCZ shifts northward leading to more rainfall in the Sahel and less rainfall in Brazil. Furthermore, the results confirm the existence of a teleconnection between the AMO and East Asian surface temperature, as well as the late withdrawal of the Indian summer monsoon, during positive AMO phases. These connections could be mainly caused by internal climate variability. Opposite patterns are true for the negative phase of the AMO.

Key words: Atlantic Multidecadal Oscillation, CMIP5, internal climate variability, climate impacts

Citation: Han, Z., F. F. Luo, S. L. Li, Y. Q. Gao, T. Furevik, and L. Svendsen, 2016: Simulation by CMIP5 models of the Atlantic Multidecadal Oscillation and its climate impacts. *Adv. Atmos. Sci.*, **33**(12), 1329–1342, doi: 10.1007/s00376-016-5270-4.

1. Introduction

The Atlantic Multidecadal Oscillation (AMO)—the leading pattern of SSTs in the North Atlantic region (Delworth and Mann, 2000; Enfield et al., 2001)—has attracted considerable attention due to its substantial climate impact. The AMO is considered to be an internal climate variability mode related to the Atlantic Meridional Overturning Circulation (AMOC), and an observable fingerprint of the AMOC (e.g. Delworth and Mann, 2000; Zhang and Delworth, 2005; Knight et al., 2006; Msadek et al., 2011; Ba et al., 2014; Drinkwater et al., 2014), although the relationship between the AMO and AMOC varies substantially from model to model (Medhaug and Furevik, 2011; Zhang and Wang, 2013). Furthermore, many model studies indicate that the AMO is also influenced by external forcing such as solar variability and volcanic and anthropogenic aerosols (Otterå et al., 2010; Chylek et al., 2011; Booth et al., 2012). Based on the 140-year instrumental record of SST, the AMO shows a dominant period of around 65–80 years (e.g., Enfield et al., 2001; Sutton and Hodson, 2007; Ting et al., 2009). However, paleoclimate and modeling studies suggest that the period of the AMO varies across a range of multidecadal timescales and encompasses more than one single defined periodicity (Gray et al., 2004; Chylek et al., 2011; Medhaug and Furevik, 2011; Ting et al., 2011).

Despite the existence of many uncertainties related to the AMO, observational and modeling studies have shown that it is associated with climate variability on the global scale, such as higher surface air temperature and decreased summer precipitation in North America (Sutton and Hodson, 2007), increased surface air temperature and summer precipitation in Europe (Sutton and Hodson, 2005), a northward shift of the Atlantic ITCZ (Knight et al., 2006; Zhang and Delworth, 2006; Ting et al., 2011), more summer rainfall in the Sa-

* Corresponding author: Feifei LUO
Email: luofeifei212@mail.iap.ac.cn

hel (Zhang and Delworth, 2006; Ting et al., 2011) and India (Goswami et al., 2006; Zhang and Delworth, 2006; Feng and Hu, 2008; Li et al., 2008; Luo et al., 2011), intensified summer rainfall in the middle-to-lower reaches of the Yangtze River, and higher surface air temperature in all four seasons in East Asia (Lu et al., 2006; Li and Bates, 2007; Wang et al., 2009). It should be noted, however, that these studies depended on either relatively short observational records, historical experiments with climate models, or models forced by observed or derived AMO SST/flux anomalies (e.g., Zhang and Delworth, 2005; Lu et al., 2006; Li et al., 2008; Yu et al., 2009). Hence, it is very hard to disentangle the climatic effects of the AMO from internal variations in the climate system (Zhang and Wang, 2013). Moreover, the AMO's associated impacts might be influenced by external forcing (Cheng et al., 2013; Chiang et al., 2013; Dunstone et al., 2013; Wilcox et al., 2013; Martin et al., 2014; Allen, 2015).

In this study, we investigate the spatiotemporal characteristics and climatic impacts of the AMO as a mode of internal variability, by comparing the "Pre-industrial Control" output of models participating in CMIP5 with observations. Following this introduction, section 2 describes the model and datasets used; section 3 compares the CMIP5-simulated AMO and related climatic patterns with observations; and finally, a summary and discussion is provided in section 4.

2. Models and data

The modeled monthly SST, surface temperature and precipitation are utilized in this study, based on the two types of simulations in CMIP5: (1) "Historical" simulations for 1850–2005, with observed forcing agents, including emissions or concentrations of well-mixed greenhouse gases, natural and anthropogenic aerosols, solar forcing and land use change (Taylor et al., 2012); (2)"Pre-industrial Control" simulations, with non-evolving and pre-industrial conditions, including prescribed well-mixed gases, natural aerosols or their precursors, and some short-lived species (Taylor et al., 2012). In the "Pre-industrial Control" simulations, solar forcing is kept constant and there are no volcanoes. Output is downloaded from the PCMDI CMIP5 website (http://pcmdi9.llnl.gov/esgf-web-fe/). The "Historical" simulations are used for the validation and selection of CMIP5 models, and the "Pre-industrial" simulations focus on the AMO's characteristics and impacts on temperature and precipitation, which indicates the internal variability of the AMO. Table 1 lists the modeling group, model name, the horizontal resolution of the oceanic and atmospheric components, and ensemble members, for each of the 25 chosen models. Additionally, the time spans of the "Pre-industrial" simulations for the six models chosen from these 25 for further analysis are also listed. Ten models are earth system models, including ocean and atmospheric chemistry and interactive land surface processes. More detailed information on the CMIP5 models and experiments can be found at http://cmip-pcmdi.llnl.gov/cmip5/experiment_design.html,and in related papers (e.g., Taylor et al., 2012).

The observational SST dataset is HadISST (Rayner et al., 2003), spanning the years 1870–2010 and gridded to 1.0° latitude by 1.0° longitude. The monthly global land temperature and precipitation for 1901–2009, on a $0.5^\circ \times 0.5^\circ$ grid, is obtained from the CRU TS 3.1 dataset (Mitchell and Jones, 2005). Given the sparse records of HadISST and CRU over the polar regions, the monthly surface temperature anomalies compiled by NASA's GISS are applied, covering the years 1880–2014 and on a $2.0^\circ \times 2.0^\circ$ grid (Hansen et al., 2006).

Before analysis, all of the model output, together with the observational data, are interpolated onto a $2.0^\circ \times 2.0^\circ$ grid using a linear interpolation scheme. To reduce the possible impacts of greenhouse gases, all of the "Historical" simulation, observation and reanalysis datasets are first detrended linearly. Then, the detrended time series are low-pass filtered with a nine-point running-mean filter to obtain low-frequency components. The degrees of freedom for the *t*-tests used throughout the study are $n/9 - 1$, where n stands for the number of samples. The AMO index is defined as the yearly averaged low-frequency SST anomaly in the North Atlantic basin (0°–60°N, 75°–7.5°W) (Enfield et al., 2001; Wang et al., 2009).

3. Results

3.1. *Model selection*

First, we evaluate (by comparing with observation) the skill of the 25 CMIP5 models in terms of their "Historical" simulations of the AMO. Spectral analysis shows that the observed AMO index exhibits one dominant period of around 50–70 years (Fig. 1a), consistent with earlier studies (e.g., Enfield et al., 2001; Kavvada et al., 2013). As for the models [Figs. 1(b)–(z)], most showdominant periods of around 10–70 years, with more than one significant peak. FGOALS-g2 and GFDL-ESM2G are the exceptions, showing no significant period on the decadal-to-multidecadal timescale. Figure 2 displays the similarities between the modeled and observed AMO index via a Taylor diagram (Taylor, 2001). It is clear that the models differ substantially in their representation of the evolution of the AMO index, exhibiting a wide range of temporal correlation coefficients from −0.3 to 0.6. This is expected, considering there is no initialization of the oceanic conditions, and the intrinsic stochastic forcing in the models. The majority of the models have weaker amplitudes, less than or equal to one standard deviation of the observation.

The spatial structures of the AMO in the models are compared with those in the observation (Fig. 3). Similar to many previous studies (e.g., Delworth and Mann, 2000; Zhang and Delworth, 2005; Kavvada et al., 2013; Zhang and Wang, 2013; Ba et al., 2014), the observational pattern is characterized by a horseshoe-like pattern, with a maximum center south of Greenland and east of Newfoundland in the midlatitude Atlantic (the domain represented by the black square in Fig. 3a), and with relatively weak anomalies along the coast

Table 1. Details of the 25 CMIP5 models' "Historical" simulations and six models' (in bold type) "Pre-industrial" simulations used in this paper. The model names in italic type indicate they are earth system models.

Reference number	Model name	Modeling group	Ocean (X, Y grid-points)	Atmosphere (Lon ×Lat)	Ensemble number	Timespan (yr)
1	ACCESS1.0	CSIRO-BOM, Australia	360 × 300	1.88° × 1.25°	2	—
2	ACCESS1.3	CSIRO-BOM, Australia	360 × 300	1.88° × 1.25°	2	—
3	BCC_CSM1.1	BCC, China	360 × 232	2.81° × 2.81°	3	—
4	**BCC_CSM1.1(m)**	BCC, China	360 × 232	1.13° × 1.13°	3	400
5	CCSM4	NCAR, USA	320 × 384	1.25° × 0.94°	6	—
6	*CESM1(BGC)*	NCAR, USA	320 × 384	1.25° × 0.94°	1	—
7	*CESM1(CAM5)*	NCAR, USA	320 × 384	1.25° × 0.94°	3	—
8	*CESM1(FAST CHEM)*	NCAR, USA	320 × 384	1.25° × 0.94°	3	—
9	*CESM1(WACCM)*	NCAR, USA	320 × 384	2.5° × 1.88°	1	—
10	**CNRM-CM5**	CNRM-CERFACS, France	362 × 292	1.41° × 1.41°	10	850
11	CSIROMk3.6.0	CSIRO-QCCCE, Australia	192 × 189	1.88° × 1.88°	10	—
12	FGOALS-g2	LASG, IAP, China	360 × 196	3° × 2.81°	4	—
13	*FIO-ESM*	First Institute of Oceanography, China	320 × 384	2.81° × 2.81°	3	—
14	**GFDLCM3**	NOAA GFDL, USA	360 × 210	2.5° × 2°	5	500
15	*GFDL-ESM2G*	NOAA GFDL, USA	360 × 210	2.5° × 2°	1	—
16	GISS-E2-H	NASA, USA	144 × 90	2.5° × 2°	5	—
17	*HadGEM2-CC*	Met Office Hadley Centre, UK	360 × 216	1.88° × 1.24°	1	—
18	**INM-CM4.0**	Institute for Numerical Mathematics, Russia	360 × 340	2° × 1.5°	1	500
19	IPSL-CM5A-LR	IPSL, France	182 × 149	3.75° × 1.88°	3	—
20	**IPSL-CM5A-MR**	IPSL, France	182 × 149	2.5° × 1.26°	3	300
21	IPSL-CM5B-LR	IPSL, France	182 × 149	3.75° × 1.88°	1	—
22	*MPI-ESM-LR*	Max Planck Institute for Meteorology, Germany	256 × 220	1.88° × 1.88°	3	—
23	***MPI-ESM-P***	Max Planck Institute for Meteorology, Germany	256 × 220	1.88° × 1.88°	2	1156
24	MRI-CGCM3	Meteorological Research Institute, Japan	360 × 368	1.13° × 1.13°	3	—
25	*NorESM1-ME*	Norwegian Climate Centre, Norway	320 × 384	2.5° × 1.88°	3	—

of Northwest Africa and extending westward into the tropics. Figure 4 shows the similarities between the modeled AMO patterns and that observed via a Taylor diagram (the better the model, the shorter the distance between the model and "OBS"). The skill of the different models varies greatly, represented by the wide range of spatial correlation coefficients (SCCs) (from −0.3 to 0.6) and normalized standard deviations (from 0.2 to 7.1) (Fig. 4). These diversities between the models and the observation are mainly manifested in three aspects. First, although the maximum anomalies in the models are in the mid–high latitudes, the centers depart from the observation, locating to the north or east. Second, negative anomalies can be found to the southeast of Newfoundland in some of the models. And third, the subtropical/tropical warming in most of the models is not presented in the same way as in the observation, with some of the warming situated to the north relative to that observed. These differences not only exist between the observation and the models, but also from model to model. The normalized standard deviations of some models are greater than one standard deviation of the observation, which is likely due to the strong warming around Greenland in these models (Fig. 3).

The above-mentioned analyses suggest a wide range of skill among the models in simulating the observational AMO.

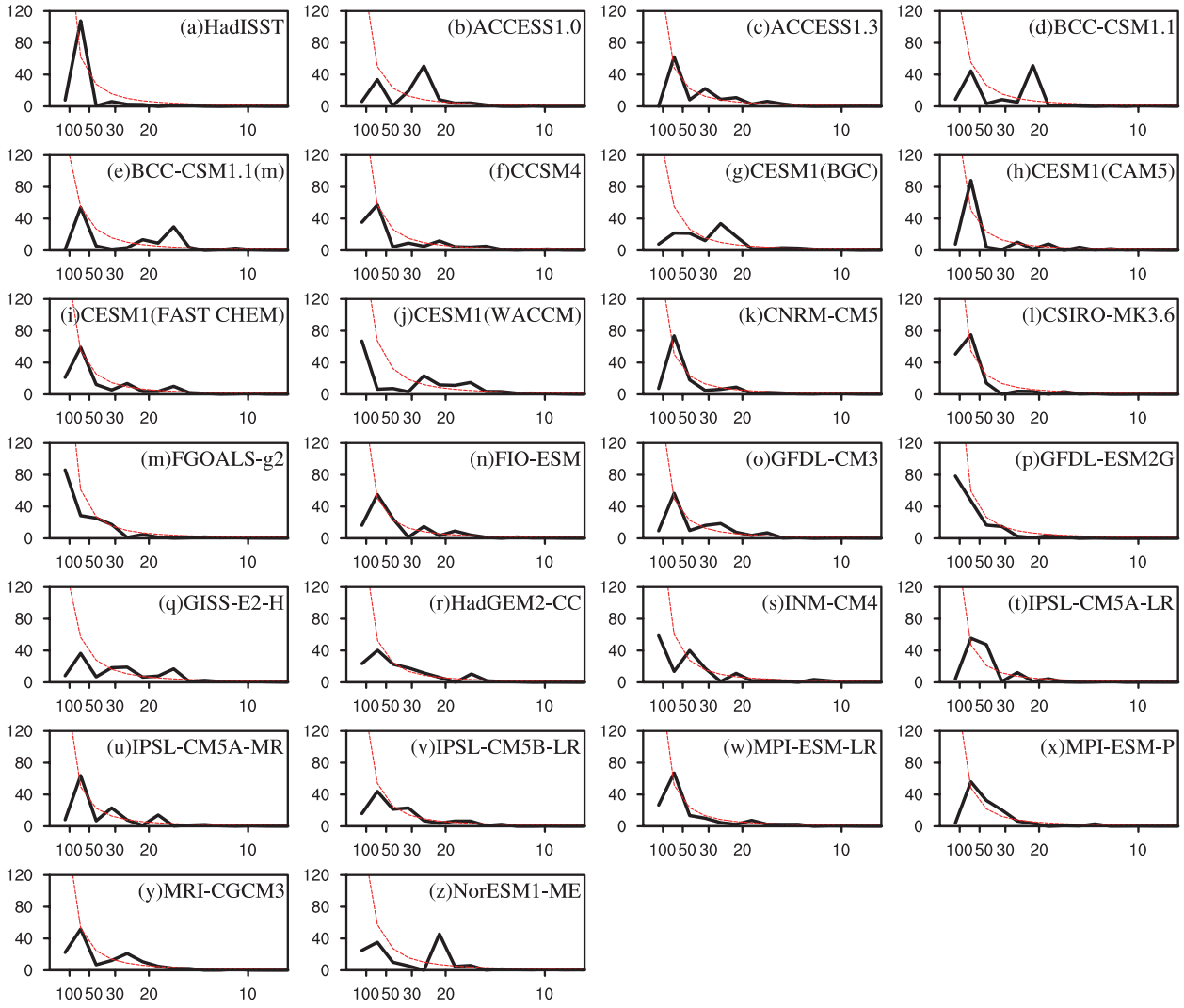

Fig. 1. Power spectrum of the AMO index for the (a) observation (HadISST) and (1–25) the models. The power spectrum is given by the black line, significant above the red line at the 5% level.

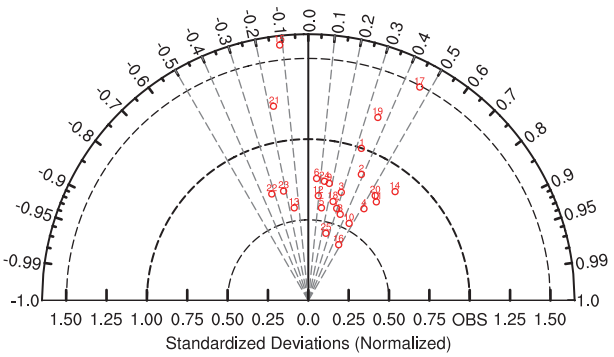

Fig. 2. Taylor diagram showing the temporal features of the AMO index for the period 1874–2001. The *x*-axis shows the normalized standard deviation and the arc shows the correlation values between observations and the ensemble mean for each model. The red numbers correspond to the model reference numbers listed in Table 1.

Model selection is based on the following criteria: (1) a significant multidecadal period; (2) a temporal normalized standard deviation within the range of ±0.5 standard deviations of the observation; (3) spatial correlations above 0.3; (4) spatial normalized standard deviations within the range of ±1 standard deviations of the observation. Table 2 summarizes the selection criteria and shows that six models qualify for selection. These six models[BCC_CSM1.1(m), CNRM-CM5, GFDLCM3, INM-CM4.0, IPSL-CM5A-MR, and MPI-ESM-P] are therefore employed to investigate the AMO-related climatic patterns in the internal natural system.

3.2. *The AMO in the "Pre-industrial" simulations*

The six models' "Pre-industrial" simulations show one dominant period of 20–70 years (Fig. 5). Compared to the period of the "Historical" simulation for each model, the period of the "Pre-industrial" simulations shows some obvious differences. For example, in the "Historical" simulation, MPI-

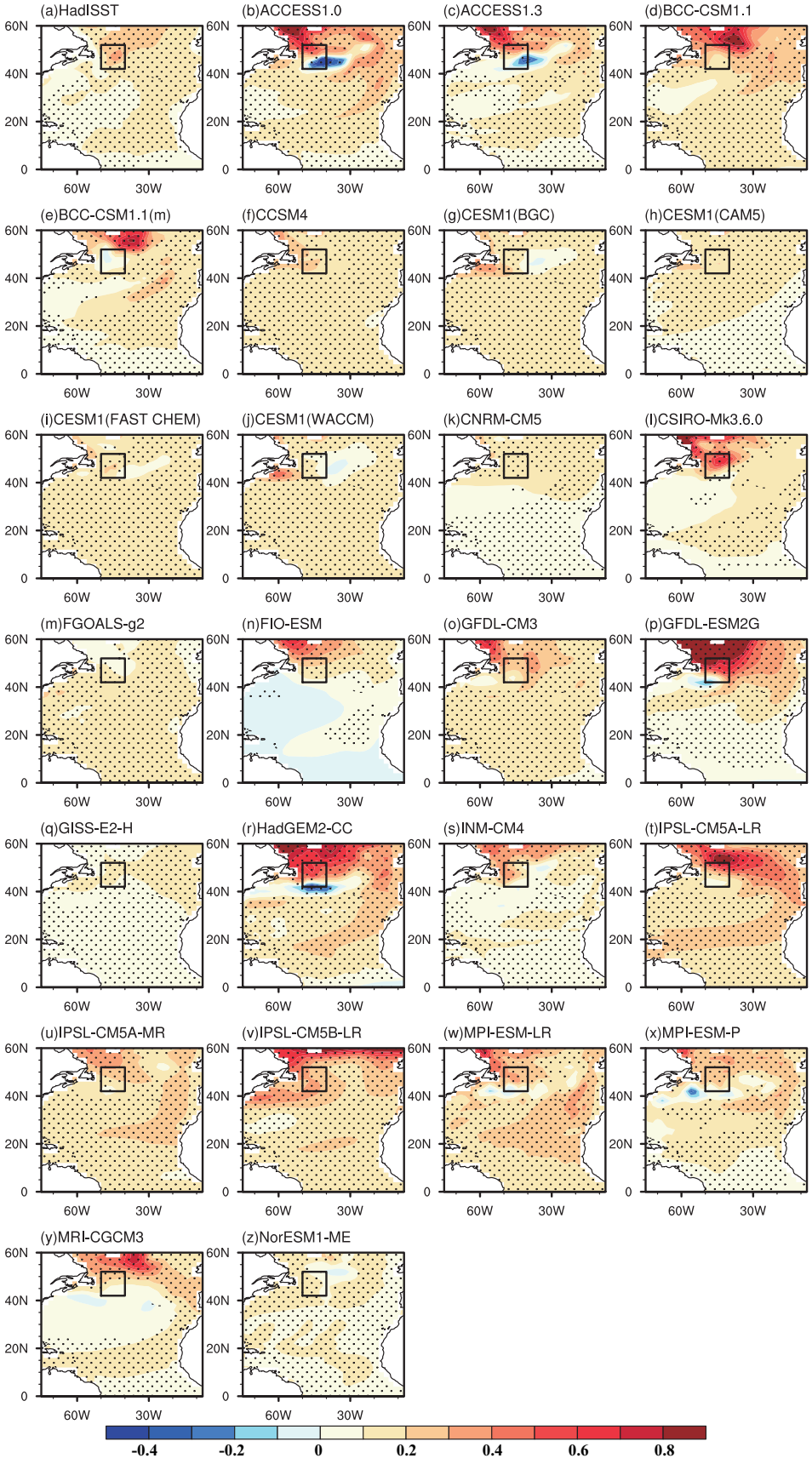

Fig. 3. Regressions of SST onto the standardized AMO index in the (a) observation and (1–25) models. Black dots indicate statistical significance at the >95% confidence level, based on the *t*-test. The black frames represent the maximum center in the observation. Units: °C.

Table 2. AMO selection criteria for the models (the six models chosen for the "Pre-industrial" simulations are in bold type). A cross indicates that: (1) the model has no significant multidecadal period (third column); (2) the temporal standard deviation of the model is outside the range of ±0.5 standard deviations of the observation (fourth column); (3) the spatial correlation between the observation and model is less than 0.3 (fifth column); and (4) the spatial standard deviation of the model is outside the range of ±1 standard deviations of the observation (sixth column).

		AMO			
		Temporal Features		Spatial Features	
Reference number	Model name	Period	Standard deviation	Correlation	Standard deviation
1	ACCESS1.0				×
2	ACCESS1.3				×
3	BCC_CSM1.1				×
4	**BCC_CSM1.1(m)**				
5	CCSM4			×	
6	CESM1(BGC)			×	
7	CESM1(CAM5)			×	
8	CESM1(FAST CHEM)			×	
9	CESM1(WACCM)			×	
10	**CNRM-CM5**				
11	CSIROMk3.6.0				×
12	FGOALS-g2	×		×	
13	FIO-ESM				×
14	**GFDLCM3**				
15	GFDL-ESM2G	×	×		×
16	GISS-E2-H		×	×	
17	HadGEM2-CC				×
18	**INM-CM4.0**				
19	IPSL-CM5A-LR				×
20	**IPSL-CM5A-MR**				
21	IPSL-CM5B-LR				×
22	MPI-ESM-LR			×	
23	**MPI-ESM-P**				
24	MRI-CGCM3				×
25	NorESM1-ME		×	×	

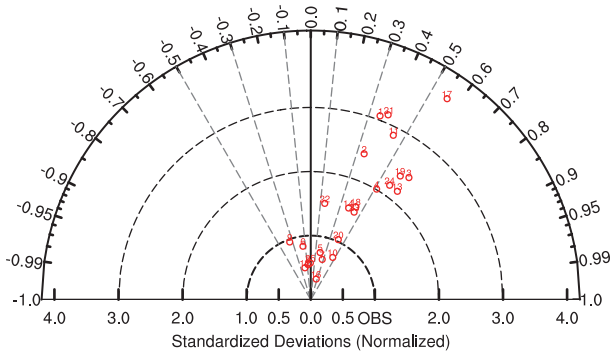

Fig. 4. Taylor diagram showing the spatial features of the regressions displayed by Fig. 3. Note that GFDL-ESM2G has a normalized standard deviation larger than 4.0 and is not shown.

ESM-P has only one peak period of around 70 years, but in the "Pre-industrial" simulation it has multiple significant multidecadal periods. The difference may be due to the different forcing conditions between the two simulations. Table 3 displays the standard deviations of the AMO index results. Both in the "Pre-industrial" and "Historical" simulations, the six modeled amplitudes are weaker than the observed amplitude (0.15°C).

Table 3. Standard deviations of the AMO index in the six selected models' "Historical" and "Pre-industrial" simulations. The standard deviation of the observed AMO index is 0.15°C. Units: °C.

Model	Historical	Pre-industrial
BCC_CSM1.1(m)	0.09	0.06
CNRM-CM5	0.08	0.10
GFDLCM3	0.12	0.09
INM-CM4.0	0.09	0.10
IPSL-CM5A-MR	0.11	0.10
MPI-ESM-P	0.10	0.12

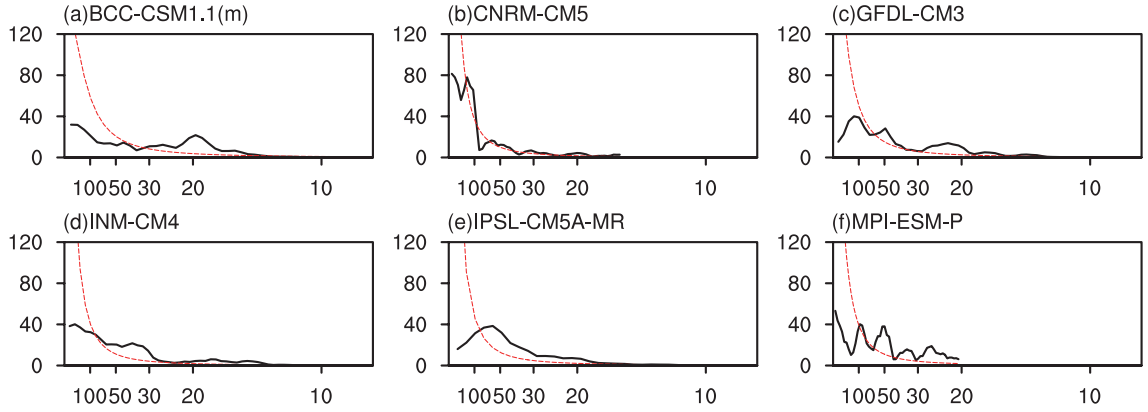

Fig. 5. Power spectrum of the AMO index for the six selected models' "Pre-industrial" simulations. The power spectrum is given by the black line, significant above the red line at the 5% level.

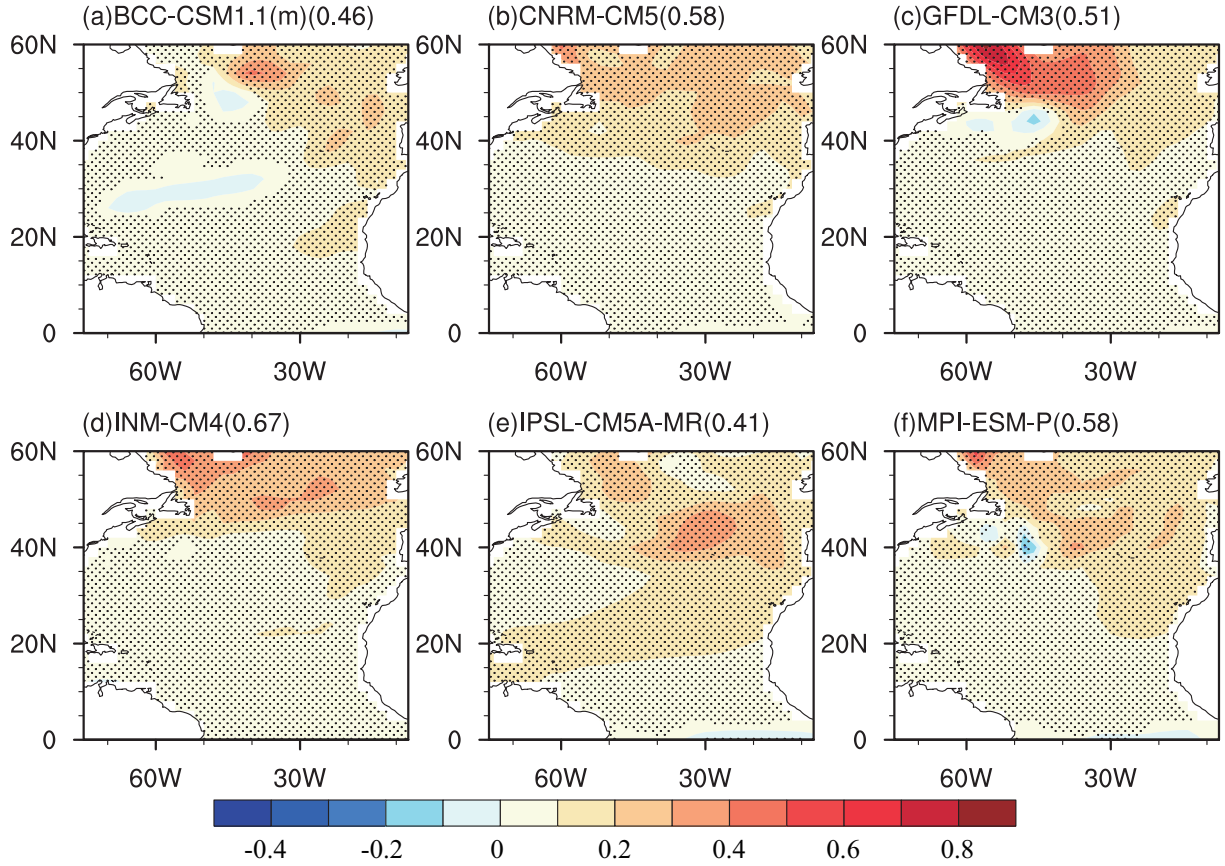

Fig. 6. Regressions of SST onto the standardized AMO index in the six selected models' "Pre-industrial" simulations. Black dots indicate statistical significance at the >95% confidence level, based on the *t*-test. Units: °C.

Figure 6 shows the spatial patterns of SST variations associated with the positive phase of the AMO in the "Pre-industrial" simulations. The differences in the spatial patterns between the "Historical" simulation and observation also exist in the "Pre-industrial" simulation. However, the "Pre-industrial" simulations still capture the essential features of the observed AMO, as indicated by the high SCCs from 0.41 to 0.67 (Fig. 6). It is interesting that the patterns in four of the six models' "Pre-industrial" simulations are closer to the observation than they are for their "Historical" simulations. These analyses indicate the existence of the AMO as an internal mode in the six models, and imply that it is rational to investigate the AMO-related climatic patterns based on these six models' "Pre-industrial" simulations.

3.3. *AMO-related climatic patterns*

3.3.1. *Surface temperature*

Figure 7 displays the AMO-related spatial patterns of surface temperature in the observations in all four seasons. On

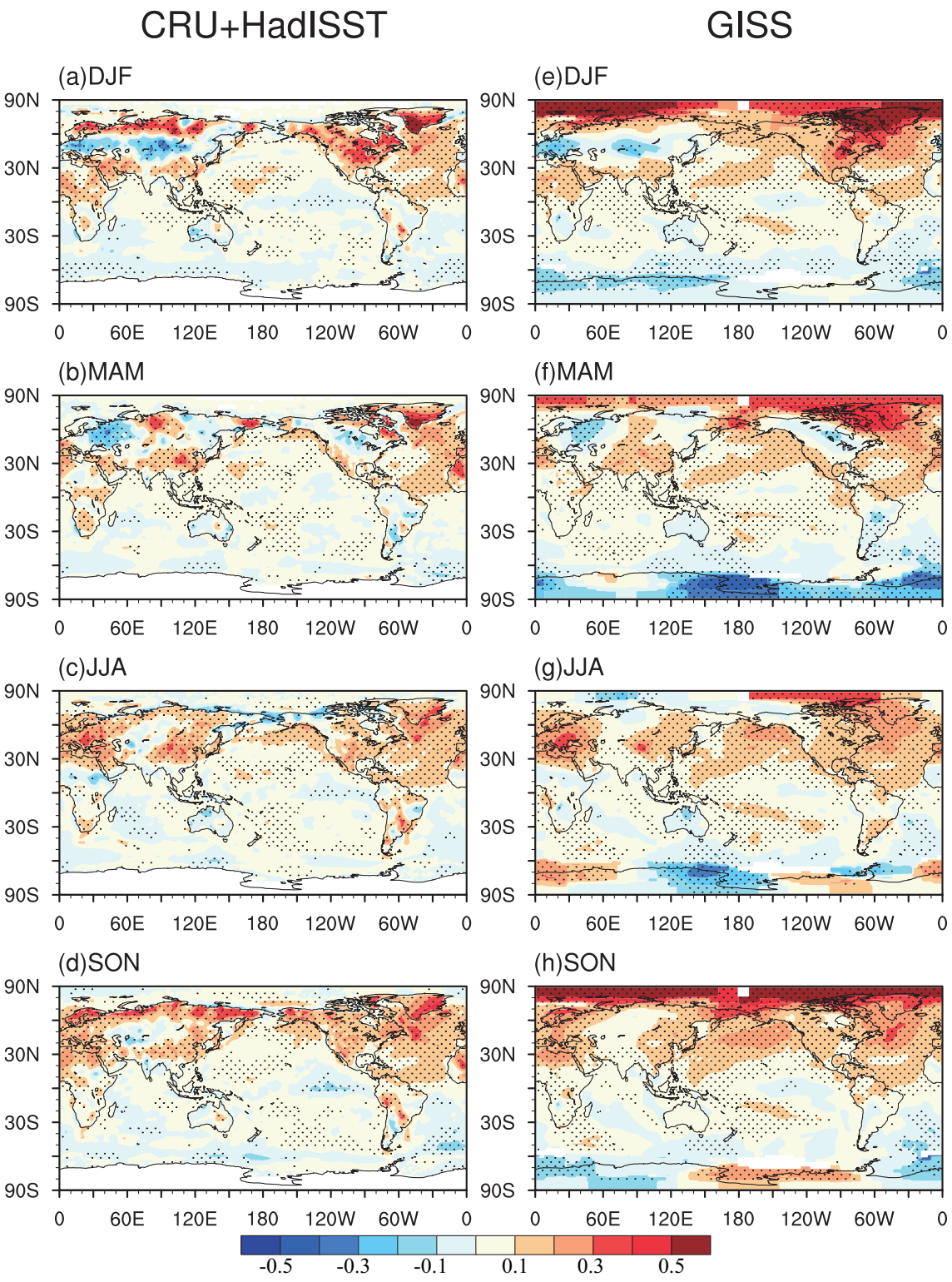

Fig. 7. Regressions of surface temperature onto the standardized AMO index: (a–d) CRU (for land temperature) and HadISST (for SST); (e–h) GISS. Black dots indicate statistical significance at the >95% confidence level, based on the *t*-test. Units: °C.

decadal-to-multidecadal timescales, oceanic thermal conditions play a key role in influencing climate variability (Bjerknes, 1964; Gulev et al., 2013). Hence, we first examine the AMO-related patterns of surface temperature in the ocean. The observations exhibit analogous spatial patterns in all seasons (Fig. 7). During positive AMO phases, the SSTs show a basin-scale cooling in the South Atlantic, and a maximum close to the Weddell Sea. For the Pacific, the observations show a tripolar pattern with positive temperature anomalies in the North and South Pacific, and slightly negative temper-

ature anomalies in the equatorial Pacific (Dong et al., 2006). For the Indian Ocean, there is a warm signal in both HadISST (Figs. 7a–d) and GISS (Figs. 7e–h), though the area of significance is much smaller in the former than the latter.

As for the AMO-related surface temperature over land, we focus on the Northern Hemisphere, considering the larger impact on the Northern Hemisphere than the Southern Hemisphere and the lower reliability of the data for the Southern Hemisphere compared with the Northern Hemisphere for the first half of the 1900s. Observations show increased temperatures over Greenland in all four seasons, maximum anomalies in winter, and minimum anomalies in summer (Fig. 7). Warming appears over the whole of the North American continent in winter, summer and autumn, while there is an east–west dipolar pattern with cooling over eastern North America and warming over western North America in spring (Fig. 7). Warming can be found over North Africa in all seasons except summer (Fig. 7). In winter, a tripolar pattern is apparent, characterized by warm–cold–warm anomalies from north to south over Eurasia (Figs. 7a and e). In spring, the anomalies exhibit an east–west pattern, with cooling over Europe and warming over most of Asia (Figs. 7b and f). In summer and autumn, Europe and eastern Asia show positive anomalies, except for a slight cooling over central Asia (Figs. 7c–h). In addition, a dipolar seesaw of the surface temperature over the Arctic and Antarctic is apparent in GISS in winter and spring (Chylek et al., 2010).

To illustrate the regions that have signals that agree among the six models(Figs. S1–S4 in the supporting information), we mark red/blue dots to represent the matching positive/negative regression coefficients in all of the models (Fig. 8). As can be seen, there is little similarity in the Southern Hemisphere among the models, and matchingpositive signals are present over most of the Northern Hemisphere. The AMO-related SST patterns bear no obvious seasonality and show warm anomalies over the equatorial Pacific, most of the North Pacific and Indian oceans, in addition to the North Atlantic. For the AMO-related surface temperature over land, it can be seen that there is a warming over Greenland, with a maximum extent in winter and spring and a minimum in summer. Over eastern North America and North Africa, the warming exists in all four seasons. For Eurasia, warming can be seen in all four seasons over the Scandinavian Peninsula, central Asia and eastern Asia. In particular, there is a band of warming from the Scandinavian Peninsula to East Asia in autumn.

Compared to the observations, a number of differences can be found in the models. First, the models are unable to capture the signals of the Southern Hemisphere and the negative surface temperature anomalies in the observations, such as those over western North America in spring and over Eurasia in winter and spring. Second, there is an opposite signal in the equatorial Pacific, in which the models portray positive anomalies but the observations show weakly negative anomalies. However, besides the warming in the North Atlantic, a number of similarities can be seen between the observations and models, such as the warming in the North Pacific, Greenland, Scandinavian Peninsula, most of North America, North Africa and East Asia.

3.3.2. *Precipitation*

Given that the impact of the AMO on precipitation mainly occurs in summer and autumn (e.g., Sutton and Hodson, 2005, 2007; Zhang and Delworth, 2006; Goswami et al., 2006; Wang et al., 2009; Kavvada et al., 2013), we focus here on discussing these two seasons. Figure 9 shows the spa-

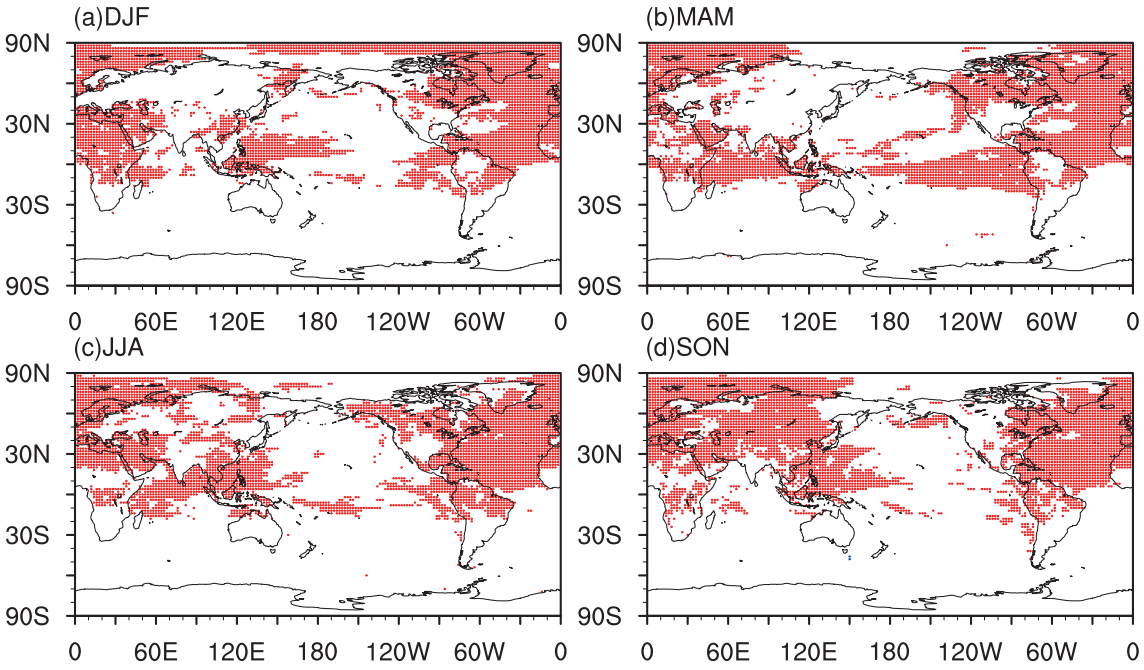

Fig. 8. Regression coefficients of surface temperature onto the AMO in each of the six selected models, where the sign of the regression agrees. Red dots indicate positive coefficients.

tial pattern of precipitation associated with positive phases of the AMO in the observation. Increased rainfall can be seen over the Sahel and north of Brazil, but decreased rainfall over Brazil, which is a result of the northward shift of the Atlantic ITCZ (Ting et al., 2011). The amplitude of rainfall over the Sahel is stronger in summer than in autumn. Less rainfall is apparent over North America in these two seasons. Europe features a dipolar pattern, with more rainfall over western Europe and less rainfall over eastern Europe in summer. There is enhanced rainfall over Siberia in summer. For the East Asian summer monsoon, a positive AMO favors intensified rainfall over East Asia, but less rainfall in autumn. In addition, there is more rainfall over India in the two seasons, which indicates a late withdrawal of the Indian summer monsoon (Lu et al., 2006; Luo et al., 2011).

Similar to Fig. 8, Fig. 10 displays signals of precipitation in the six models (Figs. S5–S6 in the supplementary materials) that agree. Relative to surface temperature, however, the precipitation signals are less distinct. Enhanced precipitation is situated north of the equator over the Atlantic, implying a northward shift of the Atlantic ITCZ. More rainfall can be seen over the North Atlantic, Caribbean Sea and tropical eastern Pacific, which is related to the warming in these regions. Moreover, the models produce precipitation patterns that resemble the observed patterns of more rainfall over the Sahel and less rainfall over Brazil, and the late withdrawal of the Indian summer monsoon. However, more rainfall is apparent over Europe in autumn in the models, but there is no such significant rainfall in the observation. Additionally, a number of the signals in the observation cannot be found in the models, such as the enhanced rainfall over Siberia in summer. It should also be mentioned that less rainfall over South China in summer is apparent, which is contrary to the observational results and previous studies (Lu et al., 2006; Wang et al., 2009; Yu et al., 2009). The reason is unclear and needs to be investigated further.

4. Summary and discussion

Given the difficulties involved in removing the impacts of external forcing from the AMO in instrumental records and historical simulations, the “Historical” and “Pre-industrial Control” simulations of 25 CMIP5 models are used to in-

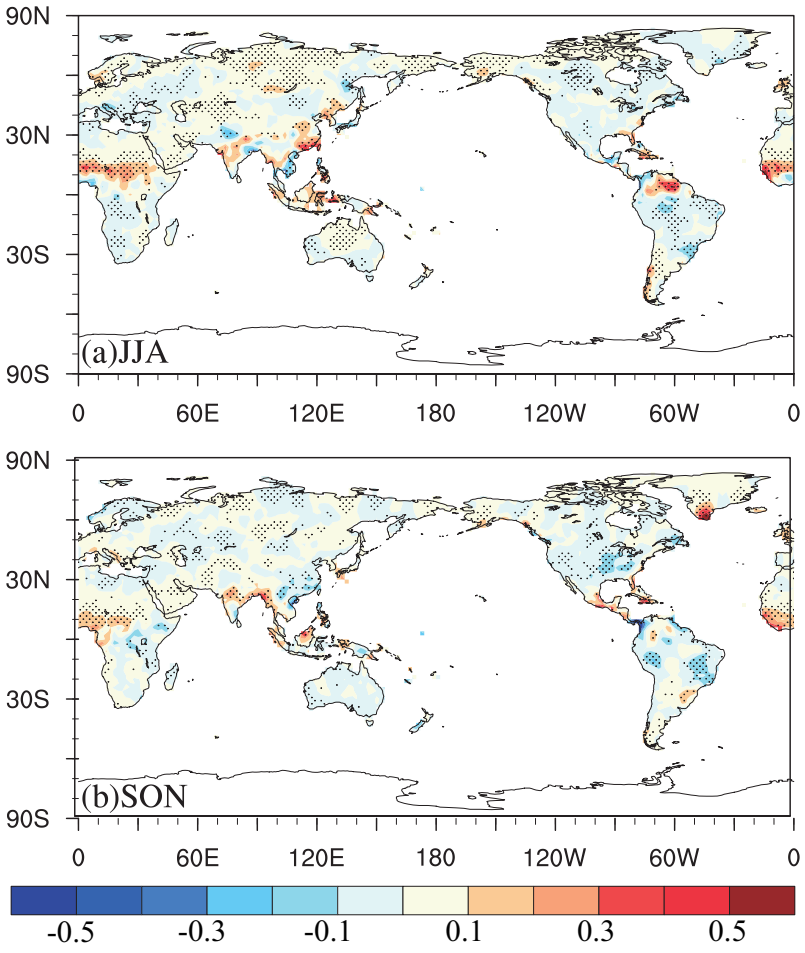

Fig. 9. Regressions of precipitation (based on CRU data) onto the standardized AMO index. Black dots indicate statistical significance at the >95% confidence level, based on the *t*-test. Units: mm d^{-1}.

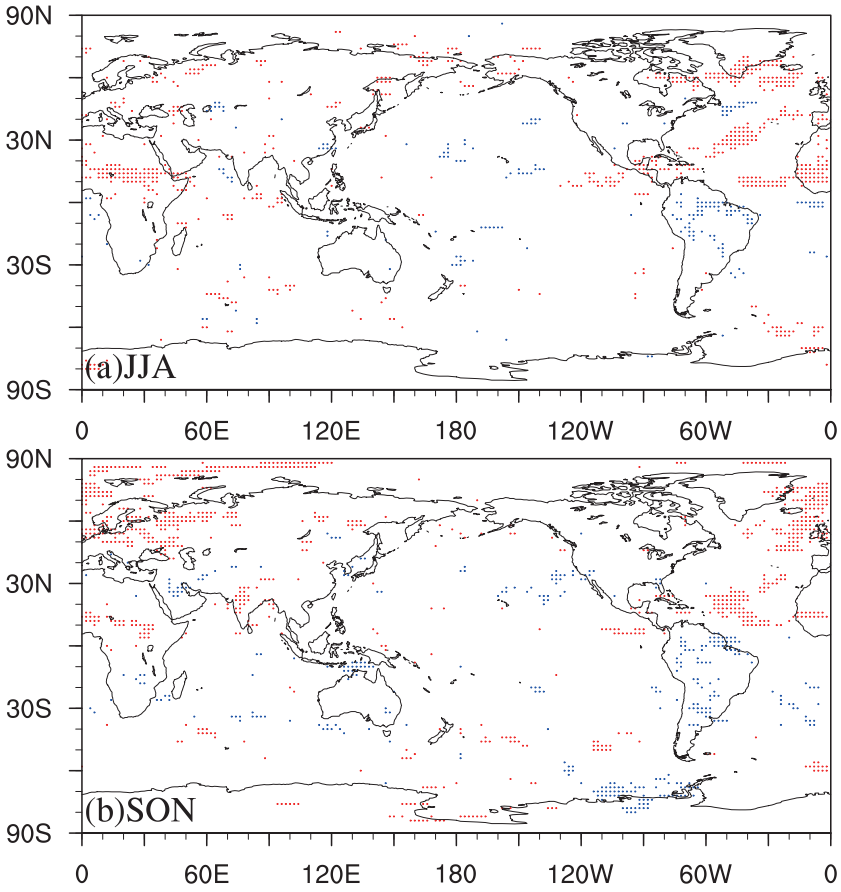

Fig. 10. Regression coefficients of precipitation onto the AMO in each of the six selected models, where the sign of the regression agrees. Red dots indicate positive coefficients, and blue dots negative.

vestigate the AMO as a mode ofinternal variability, and its associated climatic impacts. First, we assess the skill of the 25 models in simulating the observed AMO, based on their "Historical" simulations. The results suggest a wide range of skill among the models. Six models that demonstrate better skill relative to the other models are selected via certain selection criteria. The "Pre-industrial" simulations of these six models also capture the essential features of the AMO, including the multidecadal variability and basin-scale warming in the North Atlantic.

The modeled AMO-related surface temperatures show the AMO may have a larger impact on the Northern than the Southern Hemisphere. Compared to observations, the distinct difference is the opposite signals in the eastern tropical Pacific, where SSTs play an important role in AMO-related non-local impacts (Zhang and Delworth, 2005; Chen et al., 2014). As for the surface temperature over land, the main difference is that the negative anomalies over Eurasia and North America in the observations are not reproduced in the models during positive AMO phases. Nonetheless, two key similarities are found: (1) warming in the North Pacific; and (2) warming over Greenland, the Scandinavian Peninsula, North Africa, eastern North America, and East Asia.

Based on the results of the "Pre-industrial" simulations, two hypotheses are proposed. Ding et al. (2014) suggested that the recent surface warming in winter over eastern Canada and Greenland is likely caused by the natural climate variability. Here, we also show that the warming over Greenland is natural climate variability, but related to the AMO instead of LaNiña-like SST over the eastern equatorial Pacific. The recent Eurasian cooling has been suggested to be related to the Arctic sea-ice decline (e.g., Honda et al., 2009; Wu et al., 2013; Gao et al., 2015) and warming SSTs in the North Atlantic (Magnusdottir et al., 2004). However, our results imply that this recent cooling may not be relatedto the warming SSTs in the North Atlantic.

The modeled AMO-related rainfall displays a meridional shift northward of the Atlantic ITCZ, subsequently leading to more rainfall over the Caribbean Sea and the Sahel, but less rainfall over Brazil. In addition, more rainfall can be found over the North Atlantic corresponding to the magnitude of the warming there. This variability of rainfall over land as well as the increased rainfall over India in autumn in the models is consistent with that observed.

In summary, there is good agreement between the observation and models in terms of the AMO-related signals

around the North Atlantic. However, a number of differences should nevertheless be noted. The reason why the negative surface temperatures related to positive phases of the AMO observed over Eurasia and North America are not reproduced by the models remains unclear, although three possibilities are suggested as follows: The first is the model bias in simulating the backgroud atmospheric circulation. Kavvada et al. (2013) pointed out that models successfully capturing the observed features over the ocean do not necessarily also capture the observed atmospheric pattern. The second is the large difference between the models and observations in terms of the North Pacific SST anomalies,which could influence the surface temperature over North America and Europe through the atmospheric circulation (Frankignoul and Sennéchael, 2007). And the third is the limitations of the observational data due to short instrumental records, or impacts from external forcing (Suo et al., 2013).

Regarding AMO remote connections, the same signals are mainly shown for the warming in the North Pacific and East Asia, as well as the late withdrawal of the Indian summer monsoon during positive AMO phases. This is consistenet with many previous studies (Zhang and Delworth, 2005; Lu et al., 2006; Wang et al., 2009; Zhou et al., 2015). The oceanic SST anomalies may be the primary cause inducing temperature/rainfall change over East Asia/India (Lu et al., 2006; Li et al., 2008; Zhou et al., 2015). But how the AMO links to the SST variations of the North Pacific is unclear. Besides, the impact of the AMO on East Asia may be associated with the surface temperature changes from the Greenland Sea to the Kara Sea,linked to sea ice (Li et al., 2015).

The AMO-related surface temperature and precipitation patterns can be found in "Pre-industrial" simulations, which means that these may be related to internal climate variability. The AMO is considered as a vital decadal-scalepredictor because of its low-frequency nature (Keenlyside et al., 2008; Hurrell et al., 2009; Meehl et al., 2009; Kavvada et al., 2013). This study provides clues for decadal prediction in regions mainly influenced by internal climate variability, on the basis of the view that the real climate consists of natural internal variability and external forcing (Luo and Li, 2014; Steinman et al., 2015).

Acknowledgements. We acknowledge the two anonymous reviewers and Prof. Noel KEENLYSIDE for providing valuable comments on an earlier manuscript. This study was jointly supported by the National Natural Science Foundation of China (Grant No. 41421004), the National Key Basic Research Development Program of China (Grant No. 2016YFA0601802 and 2015CB453202), and the National Natural Science Foundation of China (Grant Nos. 41375085).

Electronic supplementary material. Supplementary material is available in the online version of this article at: http://dx.doi.org/10.1007/s00376-016-5270-4.

REFERENCES

Allen, R. J., 2015: A 21st century northward tropical precipitation shift caused by future anthropogenic aerosol reductions. *J. Geophys. Res. Atmos.*, **120**, 9087–9102, doi: 10.1002/2015JD023623.

Ba, J., and Coauthors, 2014: A multi-model comparison of Atlantic multidecadal variability. *Climate Dyn.*, **43**, 2333–2348, doi: 10.1007/s00382-014-2056-1.

Bjerknes, J., 1964: Atlantic air-sea interaction. *Advances in Geophysics*, **10**, 1–82.

Booth, B. B. B., N. J. Dunstone, P. R. Halloran, T. Andrews, and N. Bellouin, 2012: Aerosols implicated as a prime driver of twentieth-century North Atlantic climate variability. *Nature*, **484**, 228–232.

Chen, W., R. Y. Lu, and B. W. Dong, 2014: Intensified anticyclonic anomaly over the western North Pacific during El Niño decaying summer under a weakened Atlantic thermohaline circulation. *J. Geophys. Res. Atmos.*, **119**, 13 637–13 650, doi: 10.1002/2014JD022199.

Cheng, W., J. C. H. Chiang, and D. X. Zhang, 2013: Atlantic meridional overturning circulation (AMOC) in CMIP5 models: RCP and historical simulations. *J. Climate*, **26**, 7187–7197.

Chiang, J.-C.-H., C.-Y. Chang, and M.-F. Wehner, 2013: Long-term behavior of the Atlantic interhemispheric SST gradient in the CMIP5 historical simulations. *J. Climate*, **26**, 8628–8640.

Chylek, P., C. K. Folland, G. Lesins, and M. K. Dubey, 2010: Twentieth century bipolar seesaw of the Arctic and Antarctic surface air temperatures. *Geophys. Res. Lett.*, **37**, L08703, doi: 10.1029/2010GL042793.

Chylek, P., C. K. Folland, H. A. Dijkstra, G. Lesins, and M. K. Dubey, 2011: Ice-core data evidence for a prominent near 20 year time-scale of the Atlantic Multidecadal Oscillation. *Geophys. Res. Lett.*, **38**, L13704, doi: 10.1029/2011GL047501.

Delworth, T. L., and M. E. Mann, 2000: Observed and simulated multidecadal variability in the Northern Hemisphere. *Climate Dyn.*, **16**, 661–676.

Ding, Q. H., J. M. Wallace, D. S. Battisti, E. J. Steig, A. J. E. Gallant, H.J. Kim, and L. Geng, 2014: Tropical forcing of the recent rapid Arctic warming in northeastern Canada and Greenland. *Nature*, **509**(7499), 209–212.

Dong, B. W., R. T. Sutton, and A. A. Scaife, 2006: Multidecadal modulation of El Niño-Southern Oscillation (ENSO) variance by Atlantic Ocean sea surface temperatures. *Geophys. Res. Lett.*, **33**, L08705, doi: 10.1029/2006GL025766.

Drinkwater, K. F., M. Miles, I. Medhaug, O. H. Otterå, T. Kristiansen, S. Sundbya, and Y. Q. Gao, 2014: The Atlantic Multidecadal Oscillation: Its manifestations and impacts with special emphasis on the Atlantic region north of 60°N. *Journal of Marine Systems*, **133**, 117–130.

Dunstone, N. J., D. M. Smith, B. B. B. Booth, L. Hermanson, and R. Eade, 2013: Anthropogenic aerosol forcing of Atlantic tropical storms. *Nature Geoscience*, **6**(7), 534–539.

Enfield, D. B., A. M. Mestas-Nuñez, and P. J. Trimble, 2001: The Atlantic Multidecadal Oscillation and its relation to rainfall and river flows in the continental U.S. *Geophys. Res. Lett.*, **28**(10), 2077–2080.

Feng, S., and Q. Hu, 2008: How the North Atlantic Multidecadal Oscillation may have influenced the Indian summer monsoon during the past two millennia. *Geophys. Res. Lett.*, **35**, L01707, doi: 10.1029/2007GL032484.

Frankignoul, C., and N. Sennéchael, 2007: Observed influence of North Pacific SST anomalies on the atmospheric circulation. *J. Climate*, **20**, 592–606, doi: 10.1175/JCLI4021.1.

Gao, Y. Q., and Coauthors, 2015: Arctic sea ice and Eurasian climate: A review. *Adv. Atmos. Sci.*, **32**(1), 92–114, doi: 10.1007/s00376-014-0009-6.

Goswami, B. N., M. S. Madhusoodanan, C. P. Neema, and D. Sengupta, 2006: A physical mechanism for North Atlantic SST influence on the Indian summer monsoon. *Geophys. Res. Lett.*, **33**, L02706, doi: 10.1029/2005GL024803.

Gray, S. T., L. J. Graumlich, J. L. Betancourt, and G. T. Pederson, 2004: A tree-ring based reconstruction of the Atlantic Multidecadal Oscillation since 1567 A.D. *Geophys. Res. Lett.*, **31**, L12205, doi: 10.1029/2004GL019932.

Gulev, S. K., M. Latif, N. Keenlyside, W. Park, and K. P. Koltermann, 2013: North Atlantic Ocean control on surface heat flux on multidecadal timescales. *Nature*, **499**(7459), 464–467.

Hansen, J., M. Sato, R. Ruedy, K. Lo, D. Lea, and M. Medina-Elizade, 2006: Global temperature change. *Proceedings of the National Academy of Sciences of the United States of America*, **103**, 14 288–14 293, doi: 10.1073/pnas.0606291103.

Honda, M., J. Inoue, and S. Yamane, 2009: Influence of low Arctic sea-ice minima on anomalously cold Eurasian winters. *Geophys. Res. Lett.*, **36**, L08707, doi: 10.1029/2008GL037079.

Hurrell, J. W., and Coauthors, 2009: Decadal climate prediction: Opportunities and challenges. *Proc. OceanObs'09: Sustained Ocean Observations and Information for Society*, ESA Publication, Venice, 521–533.

Kavvada, A., A. Ruiz-Barradas, and S. Nigam, 2013: AMO's structure and climate footprint in observations and IPCC AR5 climate simulations. *Climate Dyn.*, **41**(5–6), 1345–1364.

Keenlyside, N. S., M. Latif, J. Jungclaus, L. Kornblueh, and E. Roeckner, 2008: Advancing decadal-scale climate prediction in the North Atlantic sector. *Nature*, **453**: 84–88.

Knight, J. R., C. K. Folland, and A. A. Scaife, 2006: Climate impacts of the Atlantic Multidecadal Oscillation. *Geophys. Res. Lett.*, **33**, L17706, doi: 10.1029/2006GL026242.

Li, F., H. J. Wang, and Y. Q. Gao, 2015: Extratropical ocean warming and winter Arctic sea ice cover since the 1990s. *J. Climate*, **28**, 5510–5522, doi: 10.1175/JCLI-D-14-00629.1.

Li, S. L., and G. T. Bates, 2007: Influence of the Atlantic multidecadal oscillation on the winter climate of East China. *Adv. Atmos. Sci.*, **24**(1), 126–135, doi: 10.1007/s00376-007-0126-6.

Li, S. L., J. Perlwitz, X. W. Quan, and M. P. Hoerling, 2008: Modelling the influence of North Atlantic multidecadal warmth on the Indian summer rainfall. *Geophys. Res. Lett.*, **35**, L05804, doi: 10.1029/2007GL032901.

Lu, R. Y., B. W. Dong, and H. Ding, 2006: Impact of the Atlantic Multidecadal Oscillation on the Asian summer monsoon. *Geophys. Res. Lett.*, **33**, L24701, doi: 10.1029/2006GL027655.

Luo, F. F., and S. L. Li, 2014: Joint statistical-dynamical approach to decadal prediction of East Asian surface air temperature. *Science China Earth Sciences*, **57**, 3062–3072, doi: 10.1007/s11430-014-4984-3.

Luo, F. F., S. L. Li, and T. Furevik, 2011: The connection between the Atlantic Multidecadal Oscillation and the Indian summer monsoon in Bergen Climate Model Version 2.0. *J. Geophys. Res.*, **116**, D19117, doi: 10.1029/2011JD015848.

Magnusdottir, G., C. Deser, and R. Saravanan, 2004: The effects of North Atlantic SST and sea ice anomalies on the winter circulation in CCM3. Part I: Main features and storm track characteristics of the response. *J. Climate*, **17**, 857–876.

Martin, E. R., C. Thorncroft, and B. B. B. Booth, 2014: The Multidecadal Atlantic SST–Sahel rainfall teleconnection in CMIP5 simulations. *J. Climate*, **27**, 784–806.

Medhaug, I., and T. Furevik, 2011: North Atlantic 20th century multidecadal variability in coupled climate models: Sea surface temperature and ocean overturning circulation. *Ocean Science Discussions*, **8**, 353–396.

Meehl, G. A., and Coauthors, 2009: Decadal prediction: Can it be skillful? *Bull. Amer. Meteor. Soc.*, **90**, 1467–1485.

Mitchell, T. D., and P. D. Jones, 2005: An improved method of constructing a database of monthly climate observations and associated high-resolution grids. *International Journal of Climatology*, **25**, 693–712, doi: 10.1002/joc.1181.

Msadek, R., C. Frankignoul, and L. Z. X. Li, 2011: Mechanisms of the atmospheric response to North Atlantic multidecadal variability: A model study. *Climate Dyn.*, **36**, 1255–1276, doi: 10.1007/s00382-010-0958-0.

Otterå, O. H., M. Bentsen, H. Drange, and L. L. Suo, 2010: External forcing as a metronome for Atlantic multidecadal variability. *Nature Geoscience*, **3**, 688–694.

Rayner, N. A., D. E. Parker, E. B. Horton, C. K. Folland, L. V. Alexander, D. P. Rowell, E. C. Kent, and A. Kaplan, 2003: Global analyses of sea surface temperature, sea ice, and night marine air temperature since the late nineteenth century. *J. Geophys. Res.*, **108**(D14), 4407, doi: 10.1029/2002JD002670.

Steinman, B. A., M. E. Mann, and S. K. Miller, 2015: Atlantic and Pacific multidecadal oscillations and Northern Hemisphere temperatures. *Science*, **347**(6225), 988–991.

Suo, L. L., O. H. Otterå, M. Bentsen, Y. Q. Gao, and O. M. Johannessen, 2013: External forcing of the early 20th century arctic warming. *Tellus A*, **65**, 20578.

Sutton, R. T., and D. L. R. Hodson, 2005: Atlantic Ocean forcing of North American and European summer climate. *Science*, **309**, 115–118.

Sutton, R. T., and D. L. R. Hodson, 2007: Climate response to basin-scale warming and cooling of the North Atlantic Ocean. *J. Climate*, **20**, 891–907.

Taylor, K. E., 2001: Summarizing multiple aspects of model performance in a single diagram. *J. Geophys. Res*, **106**, 7183–7192.

Taylor, K. E., R. J. Stouffer, G. A. Meehl, 2012: An overview of CMIP5 and the experiment design. *Bull. Amer. Meteor. Soc.*, **93**, 485–498.

Ting, M. F., Y. Kushnir, R. Seager, and C. H.Li, 2009: Forced and internal twentieth-century SST trends in the North Atlantic. *J. Climate*, **22**, 1469–1481.

Ting, M. F., Y. Kushnir, R. Seager, and C. H. Li, 2011: Robust features of Atlantic multi-decadal variability and its climate impacts. *Geophys. Res. Lett.*, **38**, L17705, doi: 10.1029/2011GL048712.

Wang, Y. M., S. L. Li, and D. H. Luo, 2009: Seasonal response of Asian monsoonal climate to the Atlantic Multidecadal Oscillation. *J. Geophys. Res.*, **114**, D02112, doi: 10.1029/2008JD010929.

Wilcox, L. J., E. J. Highwood, and N. J. Dunstone, 2013: The influence of anthropogenic aerosol on multi-decadal variations of historical global climate. *Environmental Research Letters*, **8**(2), 024033.

Wu, B. Y., R. H. Zhang, R. D'Arrigo, and J. Z. Su, 2013: On the Relationship between winter sea ice and summer atmospheric circulation over Eurasia. *J. Climate*, **26**, 5523–5536.

Yu, L., Y. Q. Gao, H. J. Wang, D. Guo, and S. L. Li, 2009: The responses of East Asian Summer monsoon to the North Atlantic Meridional Overturning Circulation in an enhanced freshwater input simulation. *Chinese Science Bulletin*, **54**, 4724–4732, doi: 10.1007/s11434-009-0720-3.

Zhang, L. P., and C. Z. Wang, 2013: Multidecadal North Atlantic sea surface temperature and Atlantic meridional overturning circulation variability in CMIP5 historical simulations. *J. Geophys. Res. Oceans*, **118**, 5772–5791, doi: 10.1002/jgrc.20390.

Zhang, R., and T. L. Delworth, 2005: Simulated tropical response to a substantial weakening of the Atlantic thermohaline circulation. *J. Climate*, **18**, 1853–1860.

Zhang, R., and T. L. Delworth, 2006: Impact of Atlantic multidecadal oscillations on India/Sahel rainfall and Atlantic hurricanes. *Geophys. Res. Lett.*, **33**, L17712, doi: 10.1029/2006GL026267.

Zhou, X. M., S. L. Li, F. F. Luo, Y. Q. Gao, and T. Furevik, 2015: Air-sea coupling enhances the East Asian winter climate response to the Atlantic Multidecadal Oscillation. *Adv. Atmos. Sci.*, **32**(12), 1647–1659, doi: 10.1007/s00376-015-5030-x.